# *Coarse-Grained Simulations Suggest the Epsin N-Terminal Homology Domain Can Sense Membrane Curvature without Its Terminal Amphipathic Helix*

ACS NANO

www.acsnano.org

ARTICLE

# Coarse-Grained Simulations Suggest the Epsin N-Terminal Homology Domain Can Sense Membrane Curvature without Its Terminal Amphipathic Helix

Alexis Belessiotis-Richards, Stuart G. Higgins, Mark S. P. Sansom, Alfredo Alexander-Katz,* and Molly M. Stevens*

Cite This: *ACS Nano* 2020, 14, 16919–16928

Read Online

ACCESS | Metrics & More | Article Recommendations | Supporting Information

**ABSTRACT:** **Nanoscale membrane curvature is a common feature in cell biology required for functions such as endocytosis, exocytosis and cell migration. These processes require the cytoskeleton to exert forces on the membrane to deform it. Cytosolic proteins contain specific motifs which bind to the membrane, connecting it to the internal cytoskeletal machinery. These motifs often bind charged phosphatidylinositol phosphate lipids present in the cell membrane which play significant roles in signaling. These lipids are important for membrane deforming processes, such as endocytosis, but much remains unknown about their role in the sensing of membrane nanocurvature by protein domains. Using coarse-grained molecular dynamics simulations, we investigated the interaction of a model curvature active protein domain, the epsin N-terminal homology domain (ENTH), with curved lipid membranes. The combination of anionic lipids (phosphatidylinositol 4,5-bisphosphate and phosphatidylserine) within the membrane, protein backbone flexibility, and structural changes within the domain were found to affect the domain's ability to sense, bind, and localize with nanoscale precision at curved membrane regions. The findings suggest that the ENTH domain can sense membrane curvature without the presence of its terminal amphipathic α helix *via* another structural region we have denoted as H3, re-emphasizing the critical relationship between nanoscale membrane curvature and protein function.**

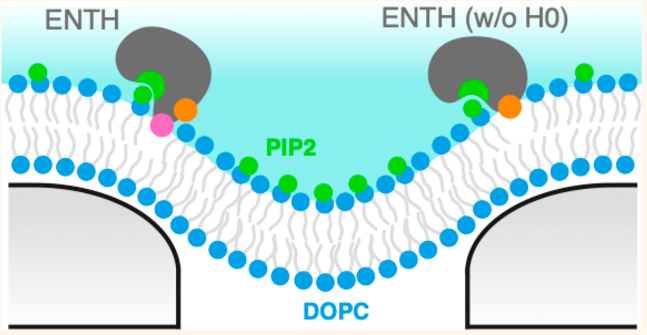


**KEYWORDS:** *membrane curvature, phosphatidylinositol 4,5-bisphosphate, molecular dynamics, coarse-grained simulations, epsin N-terminal homology domain*

The lipid membrane is a dynamic organelle of the cell required to bend and deform for a multitude of biological processes. Membrane curvature is critical for essential cellular functions such as clathrin-mediated endocytosis (CME). CME requires cytosolic proteins to bind the membrane in order to stabilize and assemble the clathrin coat.[1] A key part of this binding relies on the presence of phosphatidylinositol phosphate (PIP) lipids in the membrane, in particular phosphatidylinositol 4,5-bisphosphate (also notated PI(4,5)P2 or PtdIns(4,5)$P_2$, referred to herein as PIP2).[2] Enrichment of these lipids in the membrane is known to initiate endocytosis by recruiting early acting proteins crucial to the endocytic cascade such as Adaptor Protein 2, Fer/Cip4 homology domain only proteins 1 and 2 (FCHo1/2), assembly protein 180 kDa (AP180), and a range of epsins.[3−6] Many of these proteins contain specific PIP-binding motifs such as the pleckstrin-homology (PH) domain of FCHo, the AP180 N-terminal homology (ANTH) domain of AP180/CALM, and the epsin N-terminal homology (ENTH) domain of the epsin protein family. The individual roles of membrane curvature and phosphoinositides in endocytosis have been widely studied with respect to protein reshaping of membranes and phosphoinositide recycling in CME.[1,7−9]

Received: July 17, 2020
Accepted: December 3, 2020
Published: December 10, 2020









https://dx.doi.org/10.1021/acsnano.0c05960
*ACS Nano* 2020, 14, 16919–16928

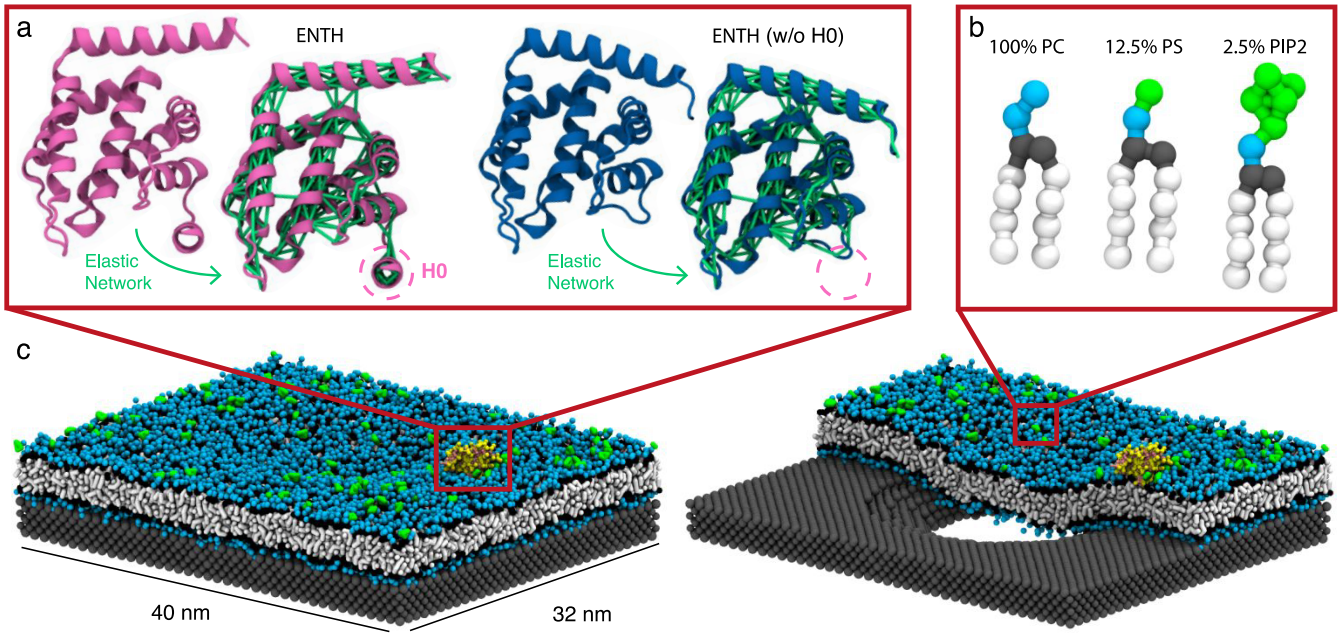


**Figure 1. (a) Crystal structures of the ENTH with (PDB code: 1H0A) and without (PDB code: 1EDU) its terminal domain α helix (H0) alongside the elastic network applied to fix secondary structure. (b) Membrane compositions used to study ENTH binding and curvature localization (100% PC, 87.5% PC + 12.5% PS, and 97.5% PC + 2.5% PIP2). The white, gray, blue, and green beads represent the hydrophobic tails, ester linkers, phosphatidylcholine headgroup, and negatively charged groups, respectively. (c) Snapshots of the simulation setup and a slice through the middle of the nanopore-deformed membrane along the *y*-axis (PIP2 lipids are highlighted in green, PC lipids are highlighted in blue).**

PIP2-binding proteins such as the Bin/amphiphysin/Rvs (BAR) domain family and septin have been the subject of extensive study for their membrane curving properties in the past decade.[10−13] However, the interplay between surface-induced membrane curvature and lipid-mediated protein binding has not been fully explored. Bioengineered nano-textured surfaces have been shown experimentally to strongly influence membrane curvature and internal cell mechanics,[14,15] hence the interest and need for supporting computational studies.

Epsins are of particular interest as some of the first proteins to engage the endocytic machinery upon membrane binding. When the ENTH crystal structure was solved by Ford *et al.*,[6] it was shown that Epsin-1 could drive membrane curvature through its ENTH domain due to the insertion of an N-terminal amphipathic α helix, referred to here as H0. The work done by Ford *et al.* suggests that this helix is formed after binding to PIP2 in the membrane. Its amphipathic nature then prefers for it to sit within the membrane itself, wedging in and creating membrane curvature. Indeed, the ENTH domain has been shown to spontaneously localize and sense membrane curvature both experimentally and in theoretical studies, and it has become a model for curvature active protein domains.[16−19] A number of reports have suggested that hydrophobic insertion of amphipathic helices is a key mechanism for membrane curvature generation in cells.[20−22] Many curvature-active proteins contain amphipathic helices such as N-BAR-containing proteins involved in endocytosis, as well as Arf1 and Sarlp.[23,24] However, recent studies suggest the exact role of such helices is more complex. Membrane composition, especially the presence of anionic lipids, plays a significant role in modulating curvature activity of amphipathic helix-containing proteins.[25−27] Chen *et al.* suggests hydrophobic residue insertion may only play a minor role in membrane curvature generation.[28] Similarly, Zeno *et al.* showed that membrane curvature sensing occurs in disordered proteins *via* purely nonspecific interactions, suggesting that electrostatic and entropic forces can drive curvature sensing without the presence of a structural sensing motif.[29] Finally, recent work by Mu *et al.* has shown that PIP2 localization to regions of membrane curvature is key to initiating an ancient Moesin-based phagocytotic pathway which is suggested to have been at the origin of receptor-mediated phagocytosis.[30] Although hydrophobic insertion is an accepted mechanism for membrane curvature sensing, it has not been explored at the molecular level in combination with PIP2. Much is unsure about the interplay between such proteins and their lipid binding partner. We have previously assumed PIP2 to be a necessary, yet neutral player in the complex act of membrane curvature sensing, but could it be that PIP2 lipids play a more active role in this process? In this work, we study a model curvature sensing protein, the ENTH domain, and its interaction not only with curvature but also with its key binding partner, PIP2. Our work presents a previously unexplored system, combining substrate-induced membrane curvature, charged phosphoinositides and proteins, allowing us to take a step closer to understanding the real-life conditions under which membrane curvature sensing occurs in the cell.

Using coarse-grained molecular dynamics simulations, we studied two crystal structures of the ENTH domain, with and without its terminal H0 helix (shown in Figure 1a). For each of these permutations, we also studied the interaction of the domains with curved phosphatidylcholine (PC) membranes containing various proportions of negatively charged lipids. The three membrane variants investigated were: pure PC, PC with 12.5% phosphatidylserine (PS), and PC with 2.5% PIP2.


https://dx.doi.org/10.1021/acsnano.0c05960
ACS Nano 2020, 14, 16919−16928

For both crystal structures, we studied how the presence and lack of a rigid elastic network, used to fix the tertiary structure of the protein domain, affected their ability to sense membrane curvature.

Following our previous work on nanopore-induced membrane deformation, our models suggest that interfacing cells with nanostructured surfaces can induce both physical as well as functional changes within the cell, potentially allowing for many applications where artificially localized cellular function would be required.[31] Understanding this relationship will allow us to posit answers to both fundamental structural and cell biology questions (for example, how important is the terminal $\alpha$ helix insertion for curvature sensing? What role does PIP2 play in curvature sensing?) and will be useful in the development of nanostructured biomaterials for both drug delivery and cell manipulation (for example, what dimensions should nanostructured surface adopt to facilitate the highest rate of cellular uptake? How does nanoscale curvature affect the local distribution of lipids and proteins in the cell membrane?).[14,32−35]

## RESULTS AND DISCUSSION

In order to study the interaction of the ENTH domain with membrane curvature, we extended our previous work on nanopore-deformed membranes.[31] We simulated three curved membrane variants containing either: neutral PC lipids, PC and 12.5% PS, or PC and 2.5% PIP2, in the upper leaflet (values shown are number percent). For cases with PS and PIP2, we ensured an equal total negative charge on the membrane surface. We allowed these membranes to interact with a negatively charged nanoporous substrate containing a central pore of 12 nm in diameter with tapered edges of 5 nm, designed to promote membrane curvature. Figure 1 shows an overview of the systems we investigated as well as snapshots of our membrane curvature model. As a control, we also studied how the ENTH domains interact with flat membranes of the same compositions. A full list of the completed simulations can be found in Table 1.

To study the role of charged lipids in curvature sensing of the ENTH domain, we selected two crystal structures of the ENTH domain, differing only in the presence or absence of the N-terminal $\alpha$ helix, H0. Figure 1a shows both crystal structures of the ENTH domain used in this study. For each crystal structure we also investigated two variants, with and without the addition of an elastic network to fix the proteins tertiary structure, giving four structures in total. The elastic network (shown in green in Figure 1a) maintains the overall tertiary and quaternary structure of the protein throughout simulations while allowing a limited degree of local flexibility. Supplementary Figure S1 compares the crystal structures of the two ENTH domains showing that the selected structures are structurally consistent, aside from the presence of H0. Throughout this work, we will refer to the ENTH domain containing its H0 helix simply as "ENTH" and the ENTH domain without H0 as "ENTH (w/o H0)". Figure 1b,c shows coarse-grained representations of the lipids used for membranes as well as snapshots of the simulation system and a slice through the membrane highlighting curvature. Supplementary Figure 2 shows more detailed snapshots of the simulation cell and a cross-section of the membrane showing its curved regions.

**Characterization of Membrane Curvature.** The curvature of our membrane system is illustrated in Figure 2a, which shows the average position of lipid heads and the corresponding evaluation of the membrane curvature profile. The radius of curvature at its peak corresponds to approximately 13 nm and is located approximately 10 nm away from the central pore. Figure 2b shows computed spatial characteristics of our curved membrane. The local PIP2 and PS density changes across the membrane, with charged lipids being enriched around regions of concave curvature in the pore center and depleted around the convex curved region. The curved membrane region around the central pore can be seen from the orientation of the lipids along the $z$-axis in Figure 2b.

**Table 1. Summary of the Simulations Carried out for This Study**

| simulation ID | protein | membrane | $N^a$ | duration ($\mu$s) |
|---|---|---|---|---|
| Curved Membrane (36 × 40 × 35 nm cell) | | | | |
| ENTH/PC | ENTH | PC | 2 × 8 | 10 |
| ENTH (w/o H0)/PC | ENTH (w/o H0) | PC | 2 × 8 | 10 |
| ENTH/PC/PIP2 | ENTH | PC/PIP2[b] | 2 × 8 | 10 |
| ENTH (w/o H0)/PC/PIP2 | ENTH (w/o H0) | PC/PIP2 | 3 × 8[d] | 10 |
| "Mutant" ENTH (w/o H0)/PC/PIP2 | ENTH (w/o H0) | PC/PIP2 | 8 | 10 |
| ENTH/PC/PS | ENTH | PC/PS[c] | 2 × 6 | 10 |
| ENTH (w/o H0)/PC/PS | ENTH (w/o H0) | PC/PS | 2 × 6 | 10 |
| Flat Membrane (20 × 20 × 20 nm cell) | | | | |
| Flat/ENTH/PC | ENTH | PC | 2 × 5 | 4 |
| Flat/ENTH (w/o H0)/PC | ENTH (w/o H0) | PC | 2 × 5 | 4 |
| Flat/ENTH/PC/PIP2 | ENTH | PC/PIP2 | 2 × 5 | 4 |
| Flat/ENTH (w/o H0)/PC/PIP2 | ENTH (w/o H0) | PC/PIP2 | 2 × 5 | 4 |
| Flat/ENTH/PC/PS | ENTH | PC/PS | 2 × 5 | 4 |
| Flat/ENTH (w/o H0)/PC/PS | ENTH (w/o H0) | PC/PS | 2 × 5 | 4 |

[a]$N$ denotes the number of simulations run. All protein simulations were performed both with and without elastic networks. [b]97.5% PC and 2.5% PIP2. [c]87.5% PC and 12.5% PS. [d]Two independent starting positions were used for the flexible ENTH (w/o H0)/PC/PIP2 simulations.

**Curvature Sensing of the ENTH Domain.** We initially placed both protein structures approximately 1.5 nm above both curved and flat membranes and let them interact under various conditions. Figure 3 shows the heat maps of the protein domains on the curved membrane seen from above, both with and without the presence of an elastic network. Figure 3 also shows the same data set as a function of radial distance from the central pore, normalized to the radial charged lipid density profile (the PC density profile is used for the case where no PIP2 or PS is present). The fold change (FC) represents the degree to which protein localization is driven by lipid density and is determined according to eq 1:

$$\text{fold change}\,(r) = \frac{\hat{f}\,(r)}{\hat{g}(r)} \tag{1}$$

where $r$ is the radial distance from the central pore, and $\hat{f}\,(r)$ is the kernel density estimator of the protein as a function of radial distance, and $\hat{g}(r)$ is the kernel density estimator of the lipid as a function of radial distance. The lipid of interest is chosen depending on the simulation case, that is, for PC-only,


https://dx.doi.org/10.1021/acsnano.0c05960
ACS Nano 2020, 14, 16919−16928

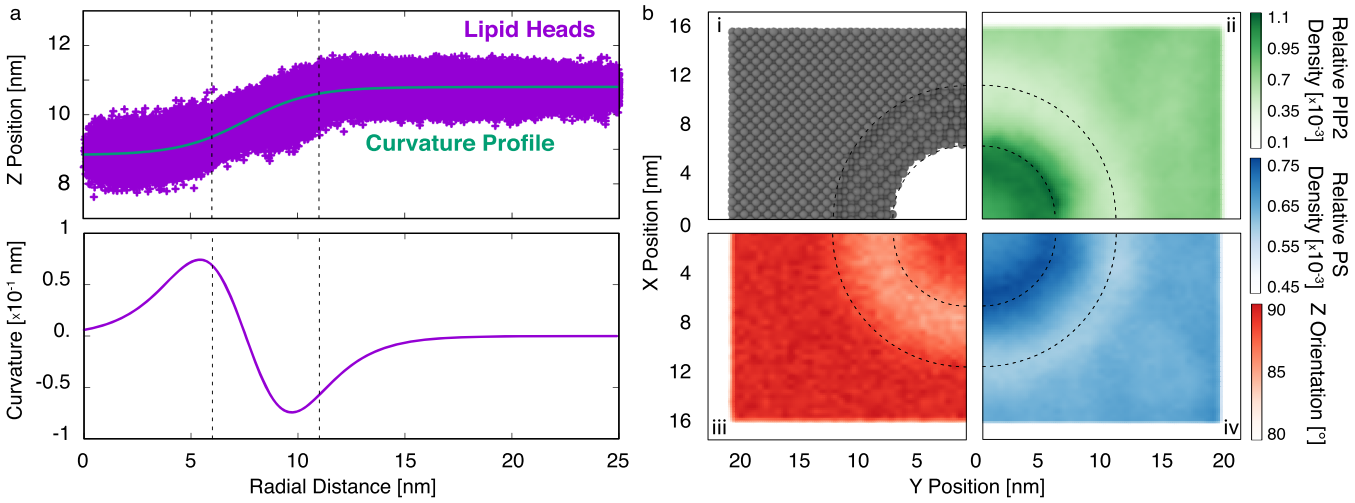


**Figure 2. Characteristics of the curved membrane showing (a) average position of PC lipid heads, curvature profile, and the computed curvature of the membrane as a function of radial distance from the central pore. (b) Heat maps showing (i) a top-down snapshot, (ii) relative PIP2 density, (iii) lipid orientation along the *x*−*y* axis defined by a vector connecting the lipid headgroup bead to its first ester bead, and (iv) PS density on the curved membrane. Dashed lines represent the start and stop of the tapered region of underlying nanoporous wafer approximating the region of membrane curvature.**

PS-containing, or PIP2-containing cases, we use the radial distribution of PC, PS, or PIP2 lipids, respectively. A fold change of one indicates that the densities of protein and lipid are equal at that given radius and suggests that the protein perfectly tracks lipid positions. Fold changes >1 indicate enhancement of protein localization, values <1 indicate reduced localization, and both indicate that protein localization is independent of lipid positions. Supplementary Figure S3 shows the raw histograms and kernel density estimates of the protein and lipid localization as a function of radial distance from which the FC is calculated.

Figure 3 illustrates the results of this modeling. In simulations using flexible ENTH domains, we consistently see strong localization to convex membrane curvature, at around 11 nm away from the central pore. The peaks in the respective fold change indicate that this enhancement is greater than any change in the underlying lipid density. This includes the expected localization on neutral PC membranes, due to the action of H0, see Figure 3a,b. Unexpectedly, neither removing H0 (Figure 3c,d), nor adding PIP2 or PS to the membrane (Figure 3e−h and Supplementary Figure S4, respectively), changes this behavior. This is contrary to the presumption that strong curvature sensitivity is reliant upon the presence of H0. Indeed, looking at the data presented in Figure 3 as a whole, we can see that flexible ENTH domains behave similarly both with and without H0. This suggests that the ENTH domain can sense membrane curvature independently from H0 *via* another structural region. Our results also suggest that the ENTH domain senses curvature more strongly when its tertiary and quaternary structure is more flexible. Simulating with an elastic network, makes the domain more rigid and reduces the strength of the curvature sensing (as indicated by smaller fold change in Figure 3b,d,h) and can even remove it entirely in the ENTH/PC/PIP2 case (Figure 3f). The rigidity of the protein means that the domain cannot adapt to curvature in order to expose its hydrophobic residues to the membrane core.

When PIP2 is added into the membrane, we observe an additional localization peak in the fold-change plots between 0 and 5 nm (Figure 3f,h). These peaks are not present in the PC-only simulations (Figure 3b,d). This is due to the local enrichment of PIP2 in the central pore as shown in Figure 2b,ii and in Supplementary Figure S3e,g. The clustering of ENTH domains to dense PIP2 regions is interesting due to its implications for endocytosis, as PIP2 is significantly enriched at endocytic sites.[1] Ford *et al.* previously showed that mutated ENTH domains (which had been altered to disrupt H0 formation) localized to endocytic sites.[6] This observed behavior was explained due to the local high concentration of PIP2 at these regions. Our simulations support this theory of localized PIP2 enrichment and suggest that similar behavior can also be explained by the activation of another curvature sensitive region in the domain when H0 is not present.

**Lipid Binding of the ENTH Domain.** The protein localization results suggest that H0 may not be the only driving force behind the ENTH domains curvature sensitivity. Domains simulated with less rigid structures appear to better sense curvature. To understand this further, we analyzed how the residues of each domain bind to PC-, PC/PIP2-, and PC/PS-containing membranes. Figure 4 shows these contacts for the first 100 residues of the domains on PC and PIP2-containing membranes (Supplementary Figure S6 shows the full contact analysis for all 160 residues of the ENTH domain). Figure 4a shows the hydrophobic contacts between the ENTH domain and the different membranes. We define a hydrophobic contact as a contact between any protein residue and the hydrophobic region of the membrane, that is, the tail group of the lipid molecules present (white colored beads in Figure 1b).

In H0 containing systems, we consistently observe hydrophobic interactions from residues 3−15 corresponding to H0, which are absent in the ENTH (w/o H0) domain. However, we also see hydrophobic interactions around residues 49−65. This second region corresponds approximately to helix 3 of the domain, which we will denote as H3 for clarity. The hydrophobic activity of this region is conserved in both flexible ENTH domain models (Figure 4a,i and iii) and elastic and flexible ENTH (w/o H0) models (Figure 4a,ii, and iv and


https://dx.doi.org/10.1021/acsnano.0c05960
ACS Nano 2020, 14, 16919−16928

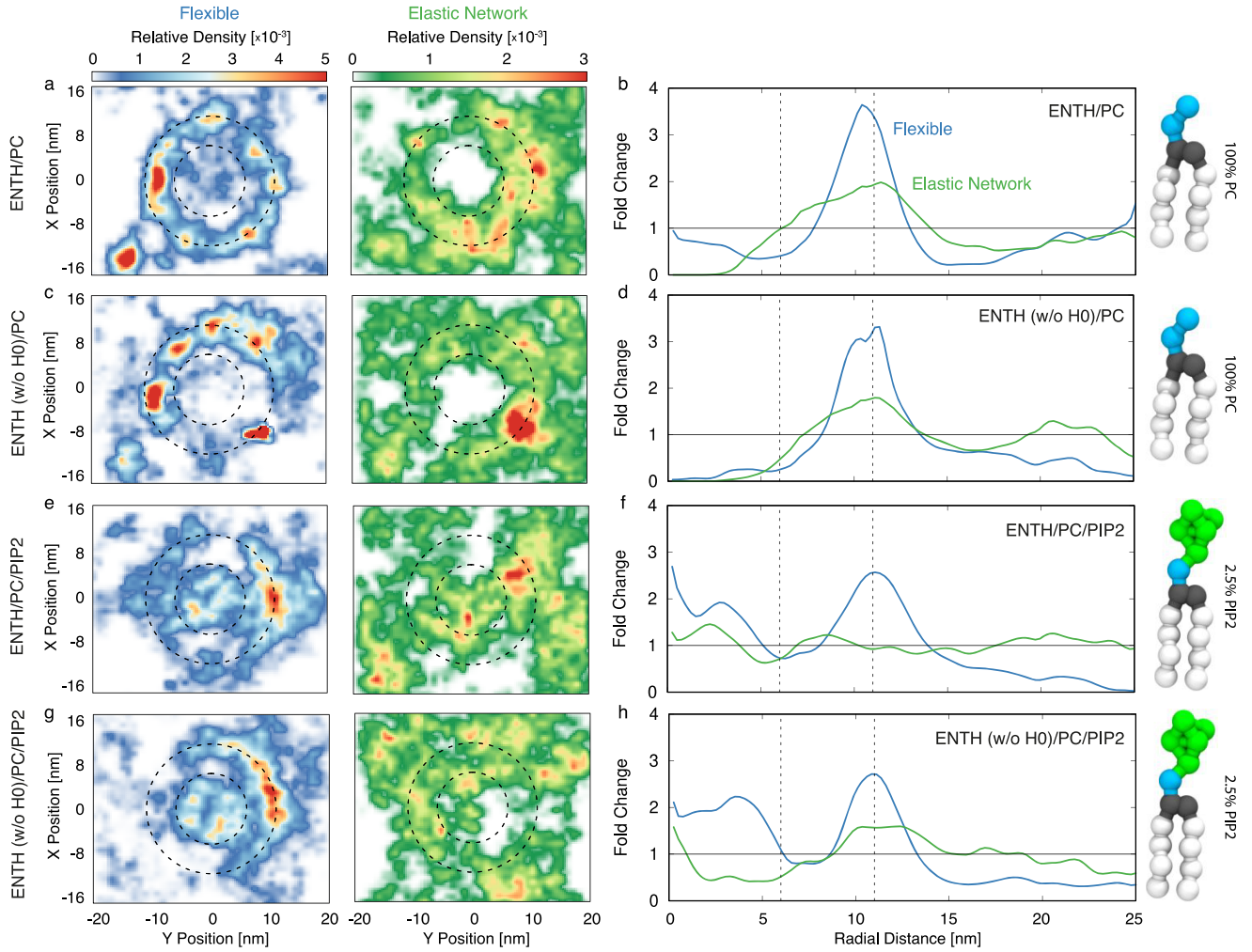


**Figure 3. Statistical frequency heat maps showing center-of-mass positions of ENTH domains and density profiles normalized to lipid density for (a,b) ENTH domain and (c,d) ENTH (w/o H0) domain interacting with a curved PC-only membrane and for (e,f) ENTH domain and (g,h) ENTH (w/o H0) domain interacting with a curved PIP2-containing membrane. Dashed lines represent the start and stop of tapered regions of underlying nanoporous wafer, approximating the region of membrane curvature.**

Supplementary Figure S7a). Conversely, simulating the domain with H0 and an elastic network results in the loss of the hydrophobic activity of H3 (Figure 4a,i and iii). Examining the sequence and structure of the ENTH domain in Supplementary Figure S8, we see that H3 has a strong hydrophobic face, more so than H0. In the elastic network ENTH (w/o H0) cases, we see the highest hydrophobic exposure at residues 48, 50, and 51 (Figure 4a,ii and iv). This corresponds to the "elbow" region of the protein which, even when the protein is left rigid, still wants to expose itself to curvature (see Supplementary Figure S8). When left flexible, H3 can fully expose itself hydrophobically, allowing for increased curvature sensing. This can be seen qualitatively in Supplementary Figure S9 which shows snapshots of flexible and elastic network ENTH domains in contact with curvature. Here, we can observe a collapse change in conformation of the flexible proteins, maximizing hydrophobic exposure, as opposed to the elastic network which is oriented away from the membrane.

These results reinforce our observations from the previous section. The ENTH domain can sense membrane curvature without the presence of H0, and our results suggest that helix 3 may be a complementary curvature-active region of this protein. When left flexible, the ENTH domain can adapt to curvature in order to expose its hydrophobic residues simultaneously (H0 and H3), allowing it to adequately sense membrane curvature. These residues give the domain its inherent curvature sensing ability. Elastic network simulations force the domain to only expose one region at a time.

From the solved crystal structure of the ENTH domain bound to PIP2, we computed the distance between the center-of-mass of the PIP2 headgroup and each residue of the protein. Figure 4b shows this distance profile, from which we can determine the binding pockets of PIP2 to the ENTH domain. Figure 4c shows PIP2 binding behavior for both ENTH and ENTH (w/o H0). Peaks are observed around residues from 0 to 10, around 30, and between 65 and 75, for both flexible and elastic network domains, consistent with the location of the binding pockets represented in Figure 4b. These results suggest that the flexible domains conserve the expected binding functionality with PIP2 (and also when interacting with PS-containing membranes, see Supplementary Figure S7).

**Structural Dynamics of the Flexible ENTH Domains.** We investigated the structural changes of the flexible ENTH domains by averaging their structures over the whole simulation ensemble for each simulation. By calculating the


https://dx.doi.org/10.1021/acsnano.0c05960
ACS Nano 2020, 14, 16919−16928

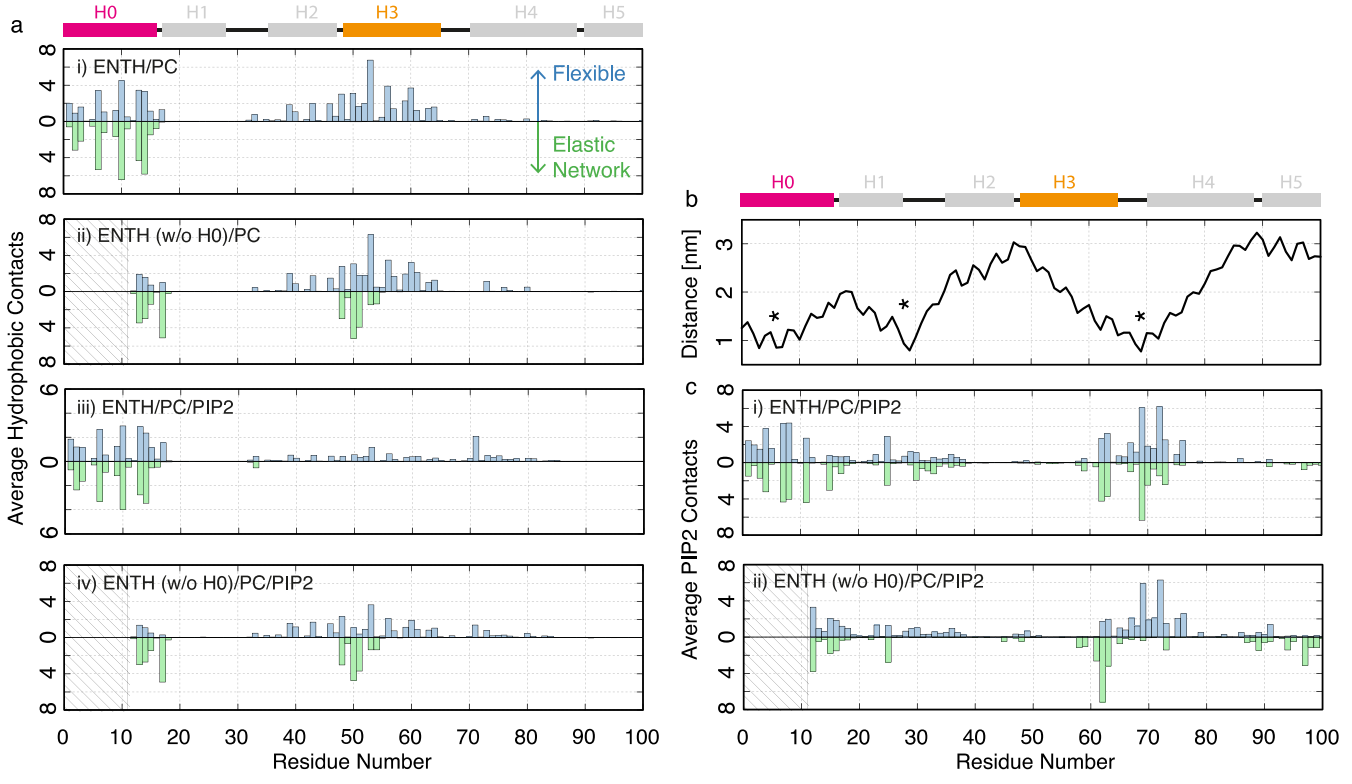


**Figure 4. Contact analysis of the first 100 residues of the ENTH domain. (a) Average number of hydrophobic contacts of the ENTH domains in contact with PC- or PC/PIP2-containing membranes. (b) Distance between the PIP2 headgroup center-of-mass and each residue of ENTH computed from the crystal structure (PDB code: 1H0A). Black asterisks represent binding pockets of PIP2. (c) Average number of contacts with PIP2 headgroup of the ENTH domains in contact with PIP2-containing membranes. A schematic of the ENTH domains secondary structure as a function of residue number is represented above the figures, and each block represents an $\alpha$ helix.**

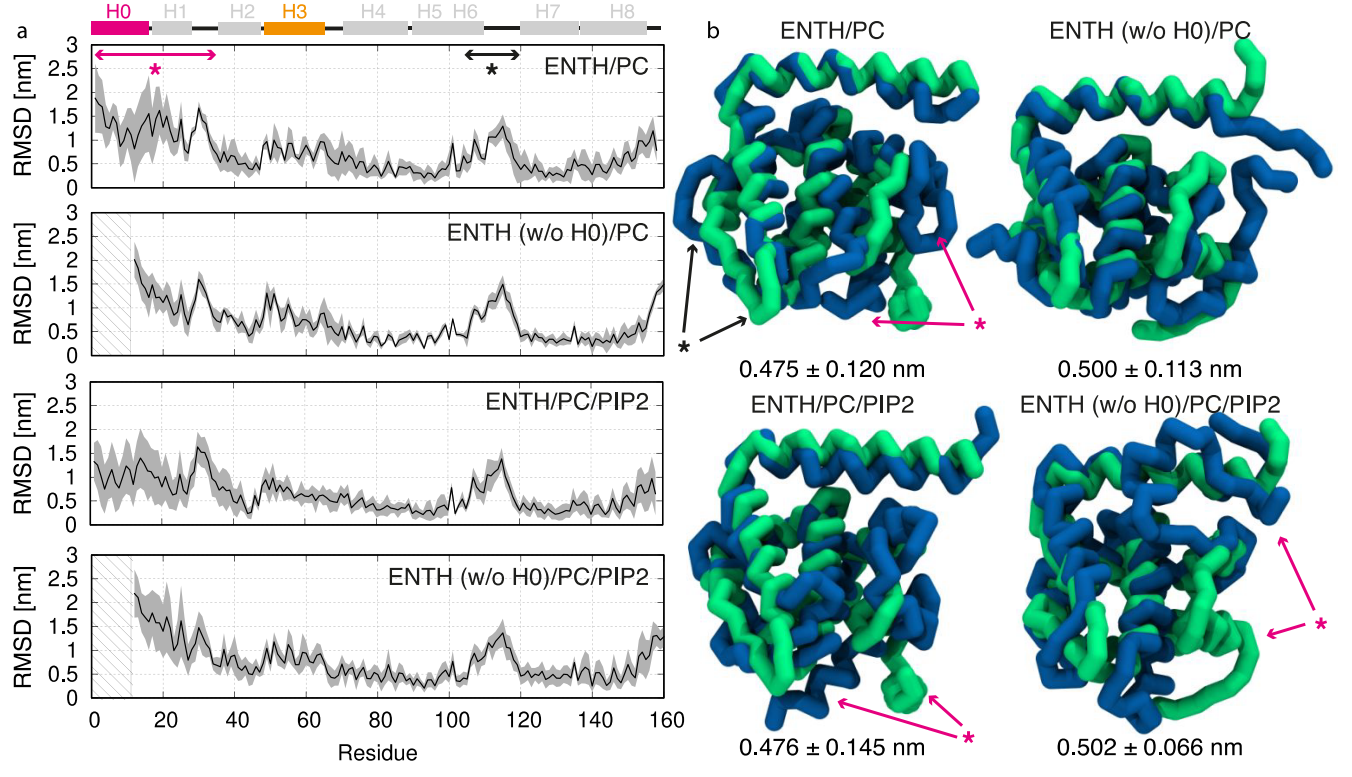


**Figure 5. (a) RMSD between flexible and elastic network ENTH domains as a function of protein residues. (b) Representative snapshots of the structures of the flexible (blue) and elastic network (green) ENTH domains with asterisks highlighting flexible regions of the protein along with the backbone RMSD difference between each structure (calculated from residues 35 to 160).**



https://dx.doi.org/10.1021/acsnano.0c05960
*ACS Nano* 2020, 14, 16919−16928

root mean squared deviation (RMSD) between the flexible and elastic network simulations, we gained insight into the dynamics and flexibility of the protein residues. Figure 5a shows the RMSD for each case as a function of residue number. Due to the lack of constraints on the protein structure in the flexible cases, we observe a fairly large RMSD per residue as expected, but we also observe consistent changes in the residue positions in two distinct regions of the protein, approximately located between residues 0 to 35 (pink asterisk in Figure 5a) and residues from 100 to 120 (black asterisk in Figure 5a). These regions are highlighted in the overlaid snapshots of the flexible and elastic network ENTH domains shown in Figure 5b and are consistently dynamic across all cases. The structures in Figure 5b are purely representative and were taken at a random time within the simulations for each case. Supplementary Figure S9 shows overlaid snapshots of the averaged structures for each simulation as well as root mean squared fluctuations (RMSF) and RMSD changes over the simulation time.

For ENTH domains with H0, this first dynamic region (residues 0−35, pink asterisk in Figure 5) can be associated with rotation/reorientation of the H0 helix in the membrane along with the associated motion of H1 and the disordered chain connecting H2. This behavior can be observed in the snapshots in Figure 5b as well as in Supplementary Figure S10 which shows more a detailed reorientation of the H0 and H1 helices for the flexible ENTH/PC/PIP2 simulations. For the ENTH (w/o H0) cases, the dynamics in this region (residues 0−35) correspond to flip-flopping of H1 and the disordered chain connecting H2. This region can flip above the domain, most likely to allow for easier exposure of H3 to the hydrophobic region of the membrane (see Figure 5b ENTH (w/o H0)/PC/PIP2 and Supplementary Figure S10). As such, we posit that the flexible simulations allow for the N-terminal region of the protein to adapt to membrane curvature, allowing either better hydrophobic insertion of H0 for the ENTH domain or closer association of H3 in the ENTH (w/o H0) domains. The second dynamic region (residues 100−120, black asterisk in Figure 5) of the protein corresponds mainly to the loop connecting helices H6 and H7. For both ENTH and ENTH (w/o H0), this loop "retreats" toward the protein core (see Figure 5b) in order to maximize hydrophobic exposure of protein residues to curvature and allow the domain to flatten onto the membrane. Both of these dynamic regions are oriented toward the membrane upon binding, and as such, each must undergo some amount deformation to maximize hydrophobic exposure of H0 and H3. Finally, we also observe a small increase in RMSD between residues 40 and 60, corresponding to H3. We can rationalize these changes as H3 is hydrophobically exposed to the membrane core.

Despite these fluctuations, we see a relatively close overlap between both the elastic and flexible structures from the snapshots in Figure 5b. This is reinforced by the backbone RMSD values (calculated from residues 35 to 160) between each structure being relatively low for such dynamic simulations (approximately 0.5 nm). This is significant, however, as the overlap between elastic and flexible domains suggests that the flexible cases are not denaturing as a whole. In fact, the flexible cases appear to retain relatively stable structural regions located between residues 35 and 100 and between residues 120 and 160. Furthermore, the curvature sensing data in Figure 3 and the PIP2-binding data in Figure 4 suggest that the observed function of the flexible domains is consistent with elastic-network structures and can even replicate observed experimental curvature sensing behavior which the latter cannot (see Figure 3e,f).

Figure 6 shows the location of H0 and H3 as well as a schematic of the ENTH domain binding to membrane

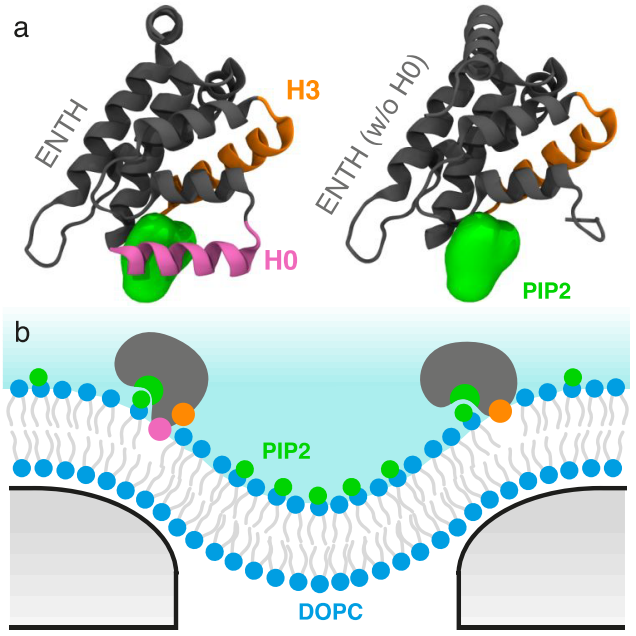


**Figure 6. (a) Structure of the ENTH domain highlighting helices H0 and H3 in pink and orange, respectively, and bound PIP2 in green. (b) Schematic overview of our work showing a cartoon ENTH domain sensing curvature both with and without H0.**

curvature with and without H0. Here, we can clearly see that when bound to PIP2, H3 is an ideal candidate for curvature sensing due to its proximity to PIP2, and as such, it will be very close to the membrane surface, and its orientation toward the membrane. Under flexible conditions, H3 can loosen itself to adequately expose its hydrophobic residues to membrane curvature, while under the elastic network, only the "elbow" of H3 can be exposed (see Supplementary Figure S8). Furthermore, without H0, the ENTH domain has ample space to orient itself in order to "flatten" onto curvature and present H3 to curvature.

## CONCLUSION

Our simulation model allows us to query functional and structural characteristics of the model curvature active ENTH domain. We have shown that we can incorporate charged signaling lipids into our membranes and characterize the binding of our domains. We have explored the effect of backbone flexibility on the curvature activity of our proteins. Surprisingly, we see that a domain can localize to curvature even without H0, the supposed curvature active region. We attribute this to the hydrophobic action of another amphipathic helix in the ENTH domain, H3, which can also sense membrane curvature. We performed all simulations both with and without an elastic network, which is typically used to fix the protein's tertiary and quaternary structure during modeling. We find that enabling backbone flexibility allows the protein to expose hydrophobic residues at regions of curvature and effectively "sense" curvature. Allowing flexibility in protein


https://dx.doi.org/10.1021/acsnano.0c05960
ACS Nano 2020, 14, 16919−16928

backbones may be useful for exploring both protein function on membranes in a computational setting as well as uncovering active structural regions in protein domains which might otherwise be locked out. There is also potential to expand our model to investigate other curvature active or lipid-binding domains to investigate their behavior on deformed membranes.

We have only focused here on substrate-induced membrane curvature, with further work required to explore the response on free-standing membranes. Free-standing membranes would be able to adapt dynamically to curvature and potentially deform spontaneously on the insertion of hydrophobic protein residues. In addition, more work is required to evaluate membranes with varying degrees of curvature, different lipid compositions, and when exposed to multiple proteins co-interacting on curvature. Furthermore, it will be important in the future to further calibrate the MARTINI force field against atomistic simulations. Here, however, we have strong experimental evidence to back up the behavior of our proteins on membrane curvature and have evaluated the dynamics on our proteins during simulation.[6,16,36]

Overall, these results open questions regarding the role of amphipathic helices in curvature sensing by proteins. The ENTH domain is arguably the first protein to be discovered to have a curvature generating function due to the action of H0 and has since served as a "gold-standard" membrane curvature protein. If the ENTH domain can sense curvature without H0, what other amphipathic helix-containing proteins might also sense curvature without it? This could be explored both computationally and experimentally in the future. Furthermore, our results begin to point toward how membranes behave when exposed to nanoscale features and the potential biological implications of both spontaneous lipid distributions as well as protein enrichment.

## METHODS

**Simulations Details.** All simulations were performed using Gromacs 4.6.7.[37] Protein simulations were performed at 323 K using the MARTINI 2 force-field with explicit water.[38] The temperature was coupled to a velocity rescale thermostat using a time constant of 1 ps, with the protein, membrane, wafer, solvent, and ions each being coupled independently. The protein crystal structures were from the RCSB protein database: ENTH with helix (Protein Data Bank (PDB) code: 1H0A) and ENTH without helix (PDB code: 1EDU). Proteins were coarse-grained using the *martinize.py* script from cgmartini.nl, and an elastic network was added, where noted, using a force constant of 500 kJ/mol and a cutoff distance of 0.9 nm. The systems were equilibrated for 20 ns using a 0.02 ps time step and a semi-isotropic Berendsen barostat using a time constant of 1 ps. For production runs, a 0.03 ps time step was used with a Parinello–Rahman barostat and a 12 ps time constant. The protein center-of-mass was computed using the *g_traj* tool, and contacts analysis was performed using the *g_mindist* tool, both in Gromacs.[37] The velocity rescaling thermostat was used throughout

**Trajectory Analysis.** All snapshots were taken using VMD.[39] The heatmaps and radial distribution histograms were computed from the protein center-of-mass (CoM) data extracted from the simulations using the *g_traj* tool mentioned above. Heatmaps in Figure 3 were created by converting the $x-y$ CoM data into absolute distances from the central pore ($x$ = 16 and $y$ = 20). These data were then mapped onto a 50 × 50 grid of equally spaced bins ($x$ limits = 0–20 nm and $y$ limits = 0–25 nm). The histograms from which the fold change is calculated were determined by converting the $x-y$ CoM data into radial distance from the central pore following:

$$r = \sqrt{(x - 16)^2 + (y - 20)^2}$$

where $r$ is the radial distance of the protein as a function of time and $x$ and $y$ are the $x$ and $y$ components of the protein CoM at a given frame. These radial data were then converted into a histogram over 100 equally spaced bins between 0 and 25 nm. In addition, kernel density estimates of the raw radial data were computed using the *stats.gaussian_kde* command from the python *scipy* package. Both the $x-y$ histograms and radial histograms were normalized so that the sum over each bin in the histogram equals 1.

**Structural Analysis.** The *g_rmsf* tool was used to compute protein residue dynamics (RMSF and RMSD), and the *g_covar* tool was used to compute average structures of the domain. The backbone RMSD values were calculated using VMD.

**Wafer Construction.** The nanoporous wafer was constructed following our previous work.[31] 40 × 40 nm PC-only, PC/PS, and PC/PIP2 membranes were first built using the *insane* tool and were sectioned into ribbons by removing 4 nm from either edge of the membrane along the $x$-direction, thereby leaving the membrane continuous only along y.[40] These were equilibrated for 20 ns and simulated for 300 ns under the same conditions mentioned above. Following this, the membranes were placed above the nanoporous wafer and again equilibrated for 20 ns and simulated for 300 ns in order to interface with the wafer. Once curved on the wafer, the unit cell was sliced from 40 × 40 nm to 32 × 40 nm in order to have a fully continuous membrane. This method ensures that we are not introducing any artificial tension in the membrane during the curving process.

## ASSOCIATED CONTENT

### Supporting Information

The Supporting Information is available free of charge at https://pubs.acs.org/doi/10.1021/acsnano.0c05960.

Additional analysis of simulations results. Supplementary Figure S1: Structural comparisons of both crystal structures used in this work. Supplementary Figure S2: Additional snapshots of the systems. Supplementary Figure S3: Raw protein localization behavior to curved membranes. Supplementary Figure S4: Localization behavior of ENTH domains to PS-containing membranes. Supplementary Figure S5: Comparison of the flexible ENTH domain simulation. Supplementary Figures S6 and S7: Binding information for all cases. Supplementary Figure S8: Sequence and secondary structure information on the ENTH domain. Supplementary Figure S9: Snapshots of the ENTH domains interacting with curvature. Supplementary Figure S10: Binding information of ENTH domains on flat membranes. Supplementary Figure S11: Structural dynamics of the ENTH domains. Supplementary Figure S12: Snapshots of the flexible ENTH domains (PDF)

## AUTHOR INFORMATION


### Corresponding Authors

**Molly M. Stevens** − *Department of Materials, Department of Bioengineering, and Institute of Biomedical Engineering, Imperial College London, London SW7 2AZ, United Kingdom;* orcid.org/0000-0002-7335-266X; Email: m.stevens@imperial.ac.uk

**Alfredo Alexander-Katz** − *Department of Materials Science and Engineering, Massachusetts Institute of Technology, Cambridge, Massachusetts 02139, United States;* Email: aalexand@mit.edu

### Authors

**Alexis Belessiotis-Richards** − *Department of Materials, Department of Bioengineering, and Institute of Biomedical*




https://dx.doi.org/10.1021/acsnano.0c05960
ACS Nano 2020, 14, 16919–16928

*Engineering, Imperial College London, London SW7 2AZ, United Kingdom;* orcid.org/0000-0001-6838-5961

**Stuart G. Higgins** − *Department of Materials, Department of Bioengineering, and Institute of Biomedical Engineering, Imperial College London, London SW7 2AZ, United Kingdom;* orcid.org/0000-0002-4653-5364

**Mark S. P. Sansom** − *Department of Biochemistry, University of Oxford, Oxford OX1 3QU, United Kingdom;* orcid.org/0000-0001-6360-7959

Complete contact information is available at: https://pubs.acs.org/10.1021/acsnano.0c05960

### Author Contributions

A.B.R. designed and carried out the simulations and the analysis. S.G.H. mentored A.B.R. and contributed to and edited the manuscript. M.S.P.S. contributed to the analysis and to the manuscript. A.A.-K. and M.M.S. supervised the research. All authors contributed to the discussion and prepared the manuscript.

### Notes

The authors declare no competing financial interest.

Raw data is available upon reasonable request from aalexand@mit.edu.

## ACKNOWLEDGMENTS

A.B.R. acknowledges a studentship from the Engineering and Physical Sciences Research Council (EPSRC) Centre for Doctoral Training in the Advanced Characterisation of Materials (EP/L015277/1). S.G.H. and M.M.S. acknowledge support from the ERC Seventh Framework Programme Consolidator Grant "Naturale CG" (616417) and a Wellcome Trust Senior Investigator Award (098411/Z/12/Z). M.S.P.S. acknowledges support from the Wellcome Trust (208361/Z/17/Z), Biotechnology and Biological Sciences Research Council (BBSRC) (BB/R00126X/1) and EPSRC (EP/R004722/1). The authors acknowledge Dr. Akemi Nogiwa Valdez for extensive proofreading and publishing support.

## REFERENCES

(1) Kaksonen, M.; Roux, A. Mechanisms of Clathrin-Mediated Endocytosis. *Nat. Rev. Mol. Cell Biol.* **2018**, *19* (5), 313−326.

(2) Antonescu, C. N.; Aguet, F.; Danuser, G.; Schmid, S. L. Phosphatidylinositol-(4,5)-Bisphosphate Regulates Clathrin-Coated Pit Initiation, Stabilization, and Size. *Mol. Biol. Cell* **2011**, *22* (14), 2588−2600.

(3) Miller, S. E.; Mathiasen, S.; Bright, N. A.; Pierre, F.; Kelly, B. T.; Kladt, N.; Schauss, A.; Merrifield, C. J.; Stamou, D.; Höning, S.; Owen, D. J. CALM Regulates Clathrin-Coated Vesicle Size and Maturation by Directly Sensing and Driving Membrane Curvature. *Dev. Cell* **2015**, *33* (2), 163−175.

(4) Kadlecova, Z.; Spielman, S. J.; Loerke, D.; Mohanakrishnan, A.; Reed, D. K.; Schmid, S. L. Regulation of Clathrin-Mediated Endocytosis by Hierarchical Allosteric Activation of AP2. *J. Cell Biol.* **2017**, *216* (1), 167−179.

(5) Henne, W. M.; Boucrot, E.; Meinecke, M.; Evergren, E.; Vallis, Y.; Mittal, R.; McMahon, H. T. FCHo Proteins Are Nucleators of Clathrin-Mediated Endocytosis. *Science (Washington, DC, U. S.)* **2010**, *328* (5983), 1281−1284.

(6) Ford, M. G. J.; Mills, I. G.; Peter, B. J.; Vallis, Y.; Praefcke, G. J. K.; Evans, P. R.; McMahon, H. T. Curvature of Clathrin-Coated Pits Driven by Epsin. *Nature* **2002**, *419* (6905), 361−366.

(7) Schöneberg, J.; Lehmann, M.; Ullrich, A.; Posor, Y.; Lo, W. T.; Lichtner, G.; Schmoranzer, J.; Haucke, V.; Noé, F. Lipid-Mediated PX-BAR Domain Recruitment Couples Local Membrane Constriction to Endocytic Vesicle Fission. *Nat. Commun.* **2017**, *8* (May), 15873.

(8) Posor, Y.; Eichhorn-Gruenig, M.; Puchkov, D.; Schöneberg, J.; Ullrich, A.; Lampe, A.; Müller, R.; Zarbakhsh, S.; Gulluni, F.; Hirsch, E.; Krauss, M.; Schultz, C.; Schmoranzer, J.; Noé, F.; Haucke, V. Spatiotemporal Control of Endocytosis by Phosphatidylinositol-3,4-Bisphosphate. *Nature* **2013**, *499* (7457), 233−237.

(9) Scott, B. L.; Sochacki, K. A.; Low-Nam, S. T.; Bailey, E. M.; Luu, Q. A.; Hor, A.; Dickey, A. M.; Smith, S.; Kerkvliet, J. G.; Taraska, J. W.; Hoppe, A. D. Membrane Bending Occurs at All Stages of Clathrincoat Assembly and Defines Endocytic Dynamics. *Nat. Commun.* **2018**, *9* (1), 273.

(10) Sorre, B.; Callan-Jones, A.; Manzi, J.; Goud, B.; Prost, J.; Bassereau, P.; Roux, A. Nature of Curvature Coupling of Amphiphysin with Membranes Depends on Its Bound Density. *Proc. Natl. Acad. Sci. U. S. A.* **2012**, *109* (1), 173−178.

(11) Prévost, C.; Zhao, H.; Manzi, J.; Lemichez, E.; Lappalainen, P.; Callan-Jones, A.; Bassereau, P. IRSp53 Senses Negative Membrane Curvature and Phase Separates along Membrane Tubules. *Nat. Commun.* **2015**, *6* (1), 8529.

(12) Simunovic, M.; Evergren, E.; Callan-Jones, A.; Bassereau, P. Curving Cells inside and Out: Roles of BAR Domain Proteins in Membrane Shaping and Its Cellular Implications. *Annu. Rev. Cell Dev. Biol.* **2019**, *35*, 111−129.

(13) Beber, A.; Taveneau, C.; Nania, M.; Tsai, F. C.; Di Cicco, A.; Bassereau, P.; Lévy, D.; Cabral, J. T.; Isambert, H.; Mangenot, S.; Bertin, A. Membrane Reshaping by Micrometric Curvature Sensitive Septin Filaments. *Nat. Commun.* **2019**, *10* (1), 420.

(14) Higgins, S. G.; Becce, M.; Belessiotis-Richards, A.; Seong, H.; Sero, J. E.; Stevens, M. M. High-Aspect-Ratio Nanostructured Surfaces as Biological Metamaterials. *Adv. Mater.* **2020**, *32* (9), 1903862.

(15) Hansel, C. S.; Crowder, S. W.; Cooper, S.; Gopal, S.; Joao Pardelha da Cruz, M.; de Oliveira Martins, L.; Keller, D.; Rothery, S.; Becce, M.; Cass, A. E. G.; Bakal, C.; Chiappini, C.; Stevens, M. M. Nanoneedle-Mediated Stimulation of Cell Mechanotransduction Machinery. *ACS Nano* **2019**, *13* (3), 2913−2926.

(16) Capraro, B. R.; Yoon, Y.; Cho, W.; Baumgart, T. Curvature Sensing by the Epsin N-Terminal Homology Domain Measured on Cylindrical Lipid Membrane Tethers. *J. Am. Chem. Soc.* **2010**, *132* (4), 1200−1201.

(17) Lai, C. L.; Jao, C. C.; Lyman, E.; Gallop, J. L.; Peter, B. J.; McMahon, H. T.; Langen, R.; Voth, G. A. Membrane Binding and Self-Association of the Epsin N-Terminal Homology Domain. *J. Mol. Biol.* **2012**, *423* (5), 800−817.

(18) Itoh, T.; Koshiba, S.; Kigawa, T.; Kikuchi, A.; Yokoyama, S.; Takenawa, T. Role of the ENTH Domain in Phosphatidylinositol-4,5-Bisphosphate Binding and Endocytosis. *Science (Washington, DC, U. S.)* **2001**, *291* (5506), 1047−1051.

(19) De Camilli, P.; Chen, H.; Hyman, J.; Panepucci, E.; Bateman, A.; Brunger, A. T. The ENTH Domain. *FEBS Lett.* **2002**, *513* (1), 11−18.

(20) Furuya, T.; Kiyota, T.; Lee, S.; Inoue, T.; Sugihara, G.; Logvinova, A.; Goldsmith, P.; Ellerby, H. M. Nanotubules Formed by Highly Hydrophobic Amphiphilic α-Helical Peptides and Natural Phospholipids. *Biophys. J.* **2003**, *84* (3), 1950−1959.

(21) Campelo, F.; McMahon, H. T.; Kozlov, M. M. The Hydrophobic Insertion Mechanism of Membrane Curvature Generation by Proteins. *Biophys. J.* **2008**, *95* (5), 2325−2339.

(22) McMahon, H. T.; Boucrot, E. Membrane Curvature at a Glance. *J. Cell Sci.* **2015**, *128* (6), 1065−1070.

(23) Bassereau, P.; Jin, R.; Baumgart, T.; Deserno, M.; Dimova, R.; Frolov, V. A.; Bashkirov, P. V.; Grubmüller, H.; Jahn, R.; Risselada, H. J.; Johannes, L.; Kozlov, M. M.; Lipowsky, R.; Pucadyil, T. J.; Zeno, W. F.; Stachowiak, J. C.; Stamou, D.; Breuer, A.; Lauritsen, L.; Simon, C. The 2018 Biomembrane Curvature and Remodeling Roadmap. *J. Phys. D: Appl. Phys.* **2018**, *51*, 343001.

(24) Drin, G.; Antonny, B. Amphipathic Helices and Membrane Curvature. *FEBS Lett.* **2010**, *584* (9), 1840−1847.

(25) Harries, D.; Ben-Shaul, A.; Szleifer, I. Enveloping of Charged Proteins by Lipid Bilayers. *J. Phys. Chem. B* **2004**, *108* (4), 1491−1496.
(26) Strandberg, E.; Zerweck, J.; Wadhwani, P.; Ulrich, A. S. Synergistic Insertion of Antimicrobial Magainin-Family Peptides in Membranes Depends on the Lipid Spontaneous Curvature. *Biophys. J.* **2013**, *104* (6), L9.
(27) Perrin, B. S.; Sodt, A. J.; Cotten, M. L.; Pastor, R. W. The Curvature Induction of Surface-Bound Antimicrobial Peptides Piscidin 1 and Piscidin 3 Varies with Lipid Chain Length. *J. Membr. Biol.* **2015**, *248*, 455.
(28) Chen, Z.; Zhu, C.; Kuo, C. J.; Robustelli, J.; Baumgart, T. The N-Terminal Amphipathic Helix of Endophilin Does Not Contribute to Its Molecular Curvature Generation Capacity. *J. Am. Chem. Soc.* **2016**, *138* (44), 14616−14622.
(29) Zeno, W. F.; Thatte, A. S.; Wang, L.; Snead, W. T.; Lafer, E. M.; Stachowiak, J. C. Molecular Mechanisms of Membrane Curvature Sensing by a Disordered Protein. *J. Am. Chem. Soc.* **2019**, *141* (26), 10361−10371.
(30) Mu, L.; Tu, Z.; Miao, L.; Ruan, H.; Kang, N.; Hei, Y.; Chen, J.; Wei, W.; Gong, F.; Wang, B.; Du, Y.; Ma, G.; Amerein, M. W.; Xia, T.; Shi, Y. A Phosphatidylinositol 4,5-Bisphosphate Redistribution-Based Sensing Mechanism Initiates a Phagocytosis Programing. *Nat. Commun.* **2018**, *9* (1), 4259.
(31) Belessiotis-Richards, A.; Higgins, S. G.; Butterworth, B.; Stevens, M. M.; Alexander-Katz, A. Single-Nanometer Changes in Nanopore Geometry Influence Curvature, Local Properties, and Protein Localization in Membrane Simulations. *Nano Lett.* **2019**, *19* (7), 4770−4778.
(32) Chiappini, C.; De Rosa, E.; Martinez, J. O.; Liu, X.; Steele, J.; Stevens, M. M.; Tasciotti, E. Biodegradable Silicon Nanoneedles Delivering Nucleic Acids Intracellularly Induce Localized *in Vivo* Neovascularization. *Nat. Mater.* **2015**, *14*, 532−539.
(33) Zhao, W.; Hanson, L.; Lou, H. Y.; Akamatsu, M.; Chowdary, P. D.; Santoro, F.; Marks, J. R.; Grassart, A.; Drubin, D. G.; Cui, Y.; Cui, B. Nanoscale Manipulation of Membrane Curvature for Probing Endocytosis in Live Cells. *Nat. Nanotechnol.* **2017**, *12* (8), 750−756.
(34) Vetrone, F.; Variola, F.; Tambasco de Oliveira, P.; Zalzal, S. F.; Yi, J.-H.; Sam, J.; Bombonato-Prado, K. F.; Sarkissian, A.; Perepichka, D. F.; Wuest, J. D.; Rosei, F.; Nanci, A. Nanoscale Oxidative Patterning of Metallic Surfaces to Modulate Cell Activity and Fate. *Nano Lett.* **2009**, *9* (2), 659−665.
(35) Lou, H. Y.; Zhao, W.; Li, X.; Duan, L.; Powers, A.; Akamatsu, M.; Santoro, F.; McGuire, A. F.; Cui, Y.; Drubin, D. G.; Cui, B. Membrane Curvature Underlies Actin Reorganization in Response to Nanoscale Surface Topography. *Proc. Natl. Acad. Sci. U. S. A.* **2019**, *116* (46), 23143−23151.
(36) Gleisner, M.; Mey, I.; Barbot, M.; Dreker, C.; Meinecke, M.; Steinem, C. Driving a Planar Model System into the 3rd Dimension: Generation and Control of Curved Pore-Spanning Membrane Arrays. *Soft Matter* **2014**, *10* (33), 6228−6236.
(37) Hess, B.; Kutzner, C.; Van Der Spoel, D.; Lindahl, E. GROMACS 4: Algorithms for Highly Efficient, Load-Balanced, and Scalable Molecular Simulation. *J. Chem. Theory Comput.* **2008**, *4* (3), 435−447.
(38) Marrink, S. J.; Risselada, H. J.; Yefimov, S.; Tieleman, D. P.; De Vries, A. H. The MARTINI Force Field: Coarse Grained Model for Biomolecular Simulations. *J. Phys. Chem. B* **2007**, *111* (27), 7812−7824.
(39) Humphrey, W.; Dalke, A.; Schulten, K. VMD: Visual Molecular Dynamics. *J. Mol. Graphics* **1996**, *14* (1), 33−38.
(40) Wassenaar, T. A.; Ingólfsson, H. I.; Böckmann, R. A.; Tieleman, D. P.; Marrink, S. J. Computational Lipidomics with *Insane*: A Versatile Tool for Generating Custom Membranes for Molecular Simulations. *J. Chem. Theory Comput.* **2015**, *11* (5), 2144−2155.


https://dx.doi.org/10.1021/acsnano.0c05960
*ACS Nano* 2020, 14, 16919−16928